



OPEN ACCESS

EDITED BY

Tamalika Banerjee,
University of Groningen, Netherlands

REVIEWED BY

Ignasi Fina,
Institute of Materials Science of
Barcelona (CSIC), Spain
Takeaki Yajima,
Kyushu University, Japan
Regina Dittmann,
Julich Research Center (HZ), Germany

*CORRESPONDENCE

Diego Rubi,
✉ diego.rubi@gmail.com

SPECIALTY SECTION

This article was submitted to
Nanoelectronics,
a section of the journal
Frontiers in Nanotechnology

RECEIVED 07 November 2022

ACCEPTED 07 December 2022

PUBLISHED 16 December 2022

CITATION

Rengifo M, Aguirre MH, Sirena M,
Lüders U and Rubi D (2022), Epitaxial
ferroelectric memristors integrated
with silicon.
Front. Nanotechnol. 4:1092177.
doi: 10.3389/fnano.2022.1092177

COPYRIGHT

© 2022 Rengifo, Aguirre, Sirena, Lüders
and Rubi. This is an open-access article
distributed under the terms of the
[Creative Commons Attribution License
\(CC BY\)](https://creativecommons.org/licenses/by/4.0/). The use, distribution or
reproduction in other forums is
permitted, provided the original
author(s) and the copyright owner(s) are
credited and that the original
publication in this journal is cited, in
accordance with accepted academic
practice. No use, distribution or
reproduction is permitted which does
not comply with these terms.

Epitaxial ferroelectric memristors integrated with silicon

Miguel Rengifo^{1,2,3}, Myriam H. Aguirre^{3,4,5}, Martín Sirena^{1,6},
Ulrike Lüders⁷ and Diego Rubi^{1,2*}

¹Instituto de Nanociencia y Nanotecnología (INN), Comisión Nacional de Energía Atómica-Consejo Nacional de Investigaciones Científicas y Técnicas (CNEA-CONICET), Buenos Aires, Argentina, ²Departamento de Micro y Nanotecnologías, Comisión Nacional de Energía Atómica (CNEA), San Martín, Argentina, ³Instituto de Nanociencia y Materiales de Aragón (INMA), Universidad de Zaragoza, Zaragoza, Spain, ⁴Departamento de Física de Materia Condensada, Universidad de Zaragoza, Zaragoza, Spain, ⁵Laboratorio de Microscopías Avanzada (LMA), Instituto de Nanociencia de Aragón (INA)-Universidad de Zaragoza, Zaragoza, Spain, ⁶Centro Atómico Bariloche and Instituto Balseiro, San Carlos de Bariloche, Río Negro, Argentina, ⁷CRISMAT, CNRS UMR 6508, ENSICAEN, Caen, France

Neuromorphic computing requires the development of solid-state units able to electrically mimic the behavior of biological neurons and synapses. This can be achieved by developing memristive systems based on ferroelectric oxides. In this work we fabricate and characterize high quality epitaxial BaTiO₃-based memristors integrated with silicon. After proving the ferroelectric character of BaTiO₃ we tested the memristive response of LaNiO₃/BaTiO₃/Pt microstructures and found a complex behavior which includes the co-existence of volatile and non-volatile effects, arising from the modulation of the BaTiO₃/Pt Schottky interface by the direction of the polarization coupled to oxygen vacancy electromigration to/from the interface. This produces remanent resistance loops with tunable ON/OFF ratio and asymmetric resistance relaxations. These properties might be harnessed for the development of neuromorphic hardware compatible with existing silicon-based technology.

KEYWORDS

memristors, neuromorphic computing, ferroelectrics, perovskites, integration with silicon

1 Introduction

Modern computers run under the Von Neumann paradigm, where the units that process and store the information are physically separated. This implies an intense data traffic between the processor (CPU) and the memory through a bus that works at a lower frequency than the CPU clock, originating the so-called “memory wall” that limits the computer performance in the case of highly demanding processes such as the training of state-of-the-art neural networks. In addition, these algorithms are extremely energy demanding suggesting that their ever-growing use in modern society might not be sustainable [Mehonic and Kenyon \(2022\)](#). This triggers the search of new computer architectures and data processing paradigms. Among them, a great deal of attention is generated by neuromorphic computing [Yu \(2017\)](#); [Mehonic and Kenyon \(2022\)](#), which intends to develop hardware beyond the Von Neumann concept, able to mimic the

extremely efficient and powerful capabilities of the mammals brain. To construct these machines, the development of solid state building blocks able to electrically replicate the behavior of neurons and synapses is needed.

Memristors—defined as metal/insulator/metal micro or nanostructures able to electrically switch between different resistance states [Sawa (2008); Ielmini and Waser (2016)]—are excellent candidates for the latter as different neuromorphic functionalities have been reported Kumar et al. (2022). Memristive mechanisms usually rely on the electromigration of charged point defects such as oxygen vacancies (OV) [(Sawa (2008); Rozenberg et al. (2010)]; however, faster devices might be expected from electronic mechanisms such as the switching of the polarization in the case of ferroelectric memristors. A lot of attention was dedicated to ferroelectric tunnel junctions (FTJs), where an ultrathin ferroelectric material is sandwiched between asymmetric metallic electrodes Tsybal and Kohlstedt (2006); Garcia et al. (2009); Zhuravlev et al. (2009); Chanthbouala et al. (2012). In this case, the direction of the (switchable) polarization controls the height of the tunnel barrier, leading to different resistive states upon polarization inversion. However, FTJs are difficult to fabricate and their response is usually extremely sensitive to the presence, for instance, of interface roughness or pin-holes in the ferroelectric layer. More robust ferroelectric memristors are found for thicker ferroelectric layers in contact with electrodes with an appropriate work-function in order to form a Schottky barrier Blom et al. (1994); Meyer and Waser (2006); Pintilie et al. (2010). In this case, the direction of the polarization modulates the height of the Schottky barrier and controls the interface resistance. For ferroelectric oxides, it was shown that the ferroelectric memristive switching is coupled to the electromigration of OV to and from Schottky interfaces Ferreyra et al. (2020a), which also influences the interface resistance. The depolarizing field (E_{DP}) was shown to play a key role in the OV dynamics. This mixture of effects was shown, for symmetric devices, to produce remanent resistance loops with distinct behavior in relation to standard (non-ferroelectric) memristors Ferreyra et al. (2020a).

An important issue linked to the development on new micro or nanoelectronic devices is their possible integration with standard Si-based technology. In the case of ferroelectric memristors, the development of epitaxial structures on Si is of paramount importance to simplify the integration with standard electronics while maintaining a high structural quality that warrants good functional properties. For instance, we recall that in polycrystalline BaTiO_3 thin films grown on platinized silicon the presence of small grain destabilizes the structural tetragonal distortion and inhibits the appearance of ferroelectricity Román et al. (2017). The obtention of epitaxial ferroelectric perovskites such as BaTiO_3 on Si was reported by using appropriate buffers that allow a better structural matching and strain accommodation between the perovskite structure and

the cubic Si cell Scigaj et al. (2013; 2016); Lyu et al. (2018). It was shown that the ferroelectric behavior is strongly linked to the perovskite fabrication conditions, which control the degree of tetragonality and, concomitantly, the remanent polarization Lyu et al. (2018).

In this work, we fabricate $\text{Si}(001)/\text{YSZ}/\text{CeO}_2/\text{LaNiO}_3/\text{BaTiO}_3/\text{Pt}$ epitaxial heterostructures and explore their memristive behavior. The high structural quality of the perovskite layers allows maintaining their bulk functional properties, namely the conducting and ferroelectric characters of LaNiO_3 and BaTiO_3 , respectively. Our devices show memristive effects controlled by the modulation of the Schottky-like BaTiO_3/Pt interface by both the direction of the ferroelectric polarization and the electromigration of oxygen vacancies to/from the interface. The combination of these effects produces a mixture of non-volatile and volatile memristive behavior that includes the existence of asymmetric resistance relaxations. The results reported here help paving the way for the development of neuromorphic hardware, integrable with standard Si technologies, as our devices can electrically replicate, in the same unit, the behavior of neurons and synapses.

2 Materials and methods

$\text{Si}(001)/\text{YSZ}/\text{CeO}_2/\text{LaNiO}_3/\text{BaTiO}_3$ multilayers were deposited by Pulsed Laser Deposition (PLD) assisted with Reflection High Energy Electron Diffraction (RHEED, 20 kV accelerating voltage was used). The optimized temperature growth and pressures were 800°C and 4.0×10^{-4} mbar for YSZ, 800°C and 4.0×10^{-4} mbar for CeO_2 , 750°C and 1.5×10^{-1} mbar for LaNiO_3 , and 750°C and 2.0×10^{-2} mbar for BaTiO_3 . The laser repetition rate and fluence were fixed at 2 Hz and 2 J/cm², respectively. Pt top electrodes were fabricated *ex-situ* from a combination of optical lithography and sputtering. The thickness and diameter of the top electrodes were 50 nm and 200 μm , respectively. X-ray diffraction experiments were performed with a Panalytical X'Pert Pro MRD diffractometer. Piezoresponse Force Microscopy (PFM) was done with a Veeco Bruker Multimode 8 microscope. Conducting Atomic Force Microscopy (CAFM) was performed with a Bruker(c) Dimension 3100 microscope. Standard atomic force microscopy (AFM) topographies were also recorded with both microscopes. The structural details of the fabricated heterostructures were analyzed by Scanning Transmission Electron Microscopy (STEM) operated in High-Angle Annular Dark Field (HAADF) mode. A FEI Titan3 60–300 microscope, coupled to a Fischione detector, was operated at 300 kV at room temperature with probe corrected beam. Strain maps were obtained by General Phase Analysis (GPA). Chemical composition was analysed by Energy Dispersive X-ray Spectroscopy (EDS). The AZTEC software was used to perform the quantifications. The estimated error in the

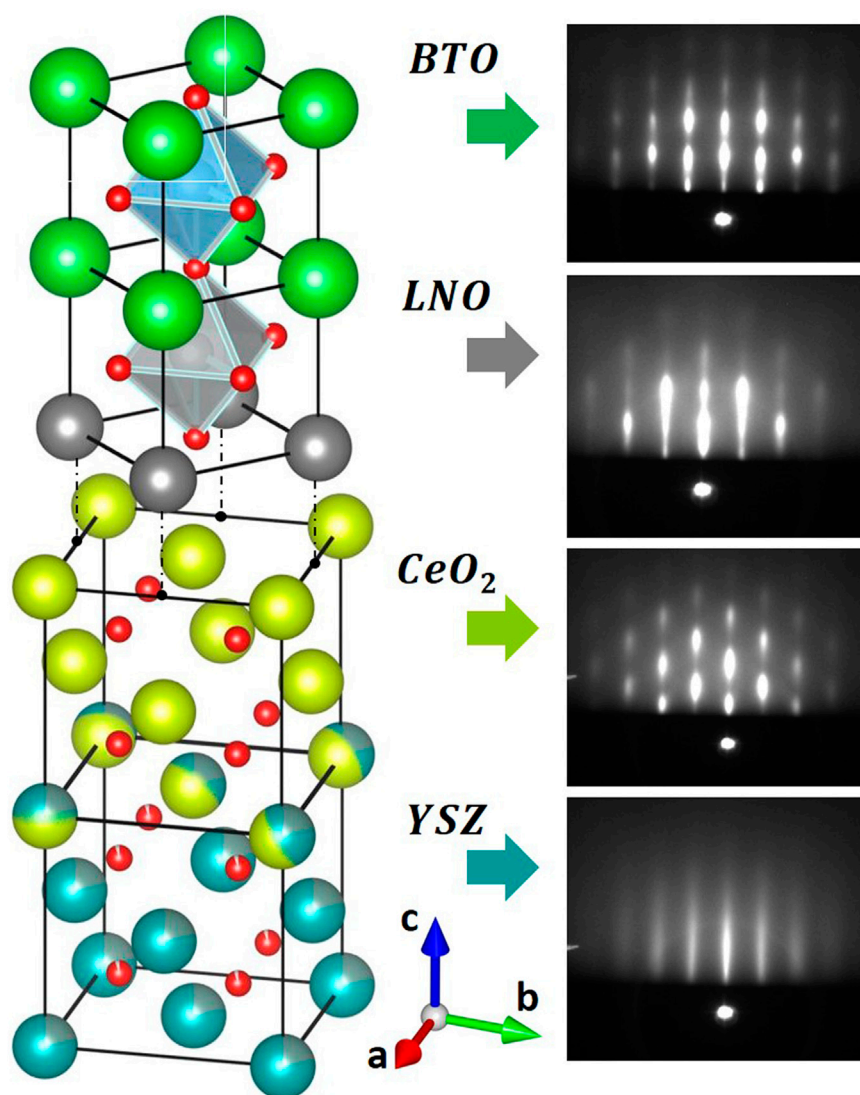


FIGURE 1

Sketch of the fabricated Si(001)/YSZ/CeO₂/LaNiO₃/BaTiO₃ heterostructure, displaying the epitaxial relations. On the right are displayed the corresponding RHEED patterns, obtained after the finalisation of the growth of each layer.

extracted atomic percentages (at%) was $\approx 2\text{--}3\%$. Electrical measurements were made at room temperature using both a Keithley 2636 Source Measure Unit and an Agilent 4294A LCR-meter, both hooked to a commercial probe station.

3 Results

3.1 Structural characterization

Yttria-stabilised zirconia (YSZ) displays a cubic structure (cell parameter $a = 0.512$ nm) and presents a lattice mismatch (defined for bottom/upper layers as $f = 100 \times (a_b - a_u)/a_b$, where a_b

and a_u are the (bulk) cell parameters of the bottom and upper layers, respectively) with Si (also cubic with cell parameter $a = 0.543$) of $f = +5.7\%$. YSZ grows epitaxially on Si without the need removing the native SiO_x layer Lubig et al. (1992) (typically ≈ 1 nm thick) that is spontaneously formed upon air exposure. The CeO₂ unit cell is also cubic (cell parameter $a = 0.541$ nm) and presents a lattice mismatch $f = -6.8\%$ with respect to YSZ. The introduction of CeO₂ buffers in our heterostructure allows accommodating the large lattice misfit existing between YSZ and the perovskite structure, and also limits the chemical reactivity of YSZ with the first perovskite layer (LaNiO₃). We notice that perovskites grow on CeO₂ with their (pseudo-)cubes ($a_{pc} \approx 0.4$ nm) rotated 45° with respect to CeO₂ cubes Scigaj et al.

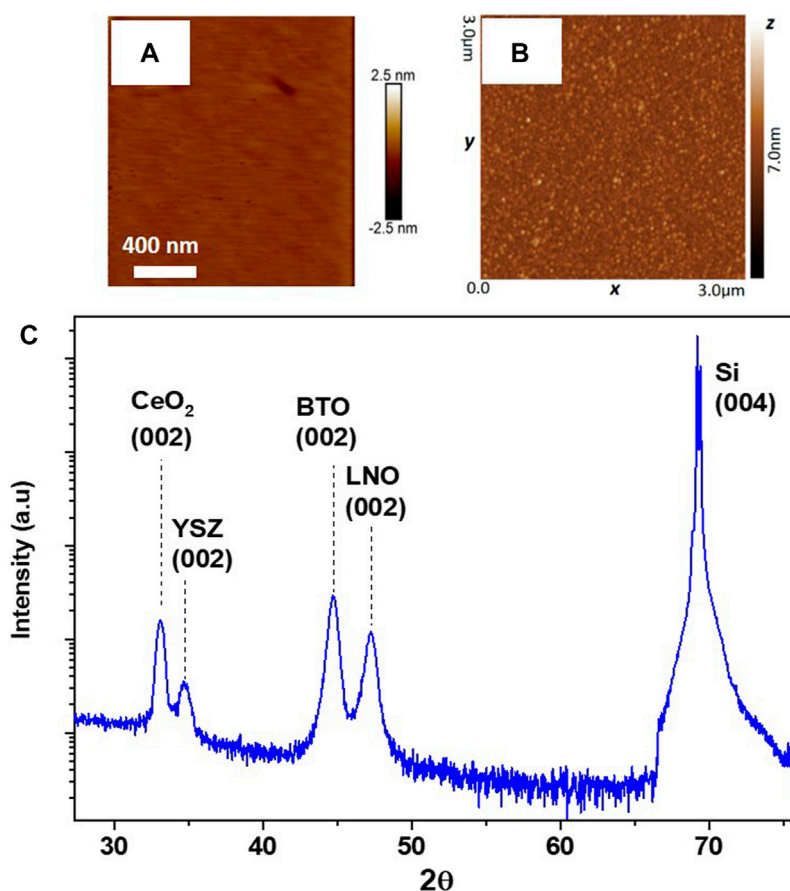


FIGURE 2

(A) Atomic force microscopy topography measured on a Si(001)/YSZ/CeO₂/LaNiO₃ structure; (B) Atomic force microscopy topography measured on a Si(001)/YSZ/CeO₂/LaNiO₃/BaTiO₃ heterostructure; (C) Bragg–Brentano X-ray diffraction pattern corresponding to a Si(001)/YSZ/CeO₂/LaNiO₃/BaTiO₃ heterostructure. LaNiO₃ and BaTiO₃ are labelled as LNO and BTO, respectively.

(2013) (we recall that $a_{pc} \approx a_{CeO_2} / \sqrt{2}$). LaNiO₃ is a metallic perovskite that crystallizes in a rhombohedral structure which can also be described by a pseudo-cubic lattice with cell parameter $a_{pc} = 0.384$ [Weber et al. (2016)]. It presents a low lattice mismatch with CeO₂, $f = +0.7\%$. BaTiO₃ displays a tetragonal structure with cell parameters $a = 0.399$ nm and $c = 0.403$ nm. It has been shown that it grows on Si(001)/YSZ/CeO₂/LaNiO₃ with an out-of-plane (001) orientation [Scigaj et al. (2016); Lyu et al. (2018)], presenting a lattice mismatch $f = -3.9\%$ with respect to LaNiO₃.

Figure 1 displays a sketch with the stack of the different layers of the Si(001)/YSZ/CeO₂/LaNiO₃/BaTiO₃ heterostructure -the epitaxial relations are [100] BaTiO₃ (001) || [100] LaNiO₃ (001) || [110] CeO₂ (001) || [110] YSZ (001) || [110] Si (001)-, together with the RHEED patterns recorded, in a single process, after the finalisation of the growth of each layer. The RHEED patterns prove the epitaxial nature of the heterostructure, in agreement with previous reports [Scigaj et al. (2013; 2016); Lyu et al. (2018)]. For YSZ and LaNiO₃ layers RHEED stripy patterns are observed,

indicating atomically flat surfaces with a root mean square (RMS) roughness of ≈ 0.5 nm. CeO₂ and BaTiO₃ layers display spotty RHEED patterns, which correspond to rougher surfaces with RMS roughness typically ≈ 1 nm. This is confirmed by the atomic force microscopy images displayed in Figures 2A,B, recorded on the LaNiO₃ and BaTiO₃ layers of the heterostructure. From these topographies we extracted RMS roughnesses of 0.5 and 0.9 nm, respectively, in good agreement with the RHEED patterns.

Figure 2C shows a Bragg-Brentano X-ray spectrum corresponding to the Si(001)/YSZ/CeO₂/LaNiO₃/BaTiO₃ heterostructure. It is found the sole presence of (002) peaks of YSZ, CeO₂, LaNiO₃ and BaTiO₃, as expected for an epitaxial heterostructure. The out-of-plane parameters (labelled as c) of the different layers have been extracted from the X-ray scan. YSZ displays an out-of-plane parameter $c = 0.516$ (1) nm, which is larger as the one corresponding to the bulk compound (0.512 nm). This suggests the presence of in-plane compressive strain, which is at odds with the tensile strain expected from the comparison of the bulk structures but is

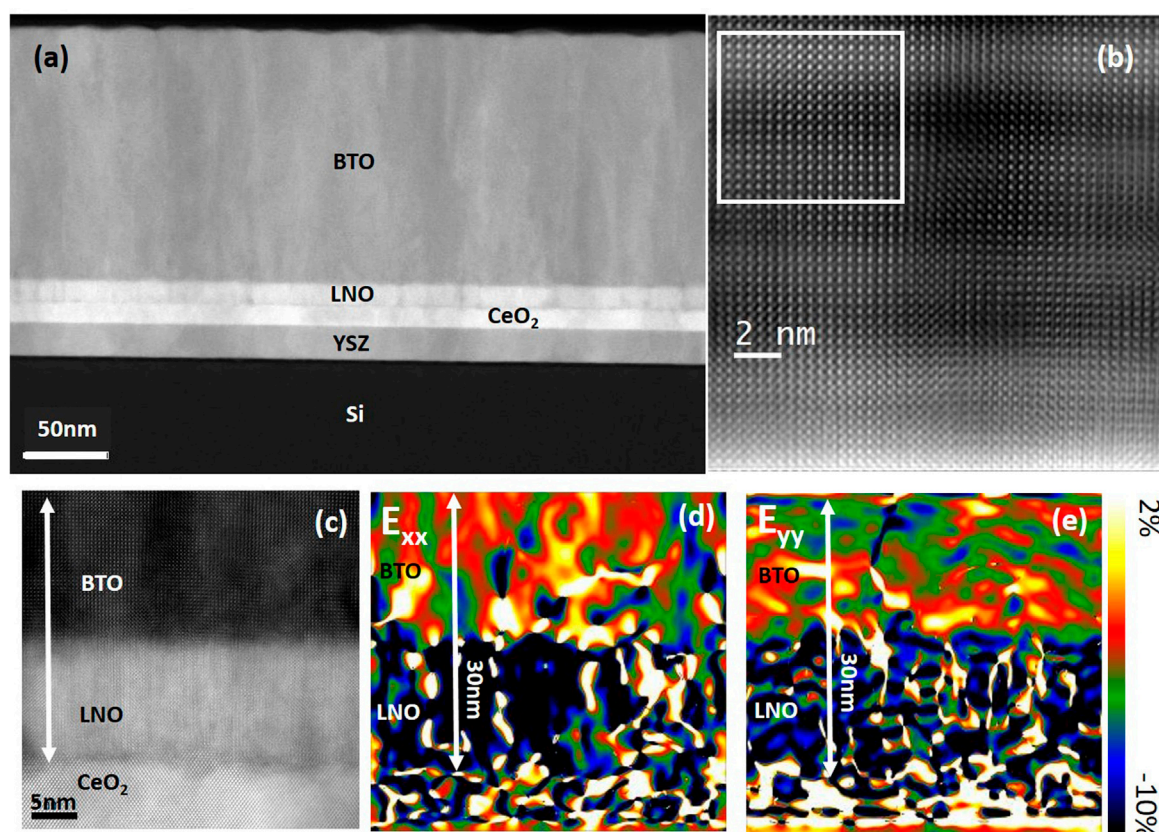


FIGURE 3

(A) Low magnification STEM-HAADF cross-section corresponding to a Si(001)/YSZ/CeO₂/LaNiO₃/BaTiO₃ heterostructure. LaNiO₃ and BaTiO₃ are labelled as LNO and BTO, respectively; (B) For the same sample, high resolution STEM-HAADF image of the BaTiO₃ layer; (C–E) In-plane (E_{xx}) and out-of-plane (E_{yy}) GPA strain maps corresponding to the LaNiO₃ and BaTiO₃ layers. See the main text for details.

consistent with previously reported GPA on similar systems Carrero et al. (2020). The presence of compressive strain on YSZ can be related to the formation of a thin SiO_x layer (≈ 3 nm, observable by high resolution STEM-HAADF images) at the Si/YSZ interface upon cooling from the deposition temperature Carrero et al. (2020). CeO₂ presents an out-of-plane parameter $c = 0.543$ (1) nm, which is slightly larger to the one corresponding to the bulk compound (0.541 nm). This is consistent with the expected in-plane compressive strain given the negative lattice mismatch between YSZ and CeO₂ bulk structures. LaNiO₃ displays an out-of-plane parameter $c = 0.383$ (1) nm, which is very close to the one of the bulk compound ($c = 0.384$), reflecting the low mismatch existing between LaNiO₃ and CeO₂ which leads to a fairly cubic perovskite unit cell Rubi et al. (2002). Finally, the out-of-plane parameter of BaTiO₃ is $c = 0.406$ (1) nm, which is larger than the bulk one (0.403 nm) and is consistent with the negative mismatch existing between LaNiO₃ and BaTiO₃.

Figure 3A displays a low magnification STEM-HAADF cross-section, where the substrate and the four layers can be visualized. All

layers present a uniform thickness (21 nm, 13 nm, 14 nm and 165 nm for YSZ, CeO₂, LaNiO₃ and BaTiO₃, respectively) and the interfaces are sharp. The STEM-HAADF analysis of the buffer layers (YSZ and CeO₂) has been already reported by some of the authors of this manuscript in Carrero et al. (2020). Both perovskite layers in our heterostructure display a columnar growth. Figure 3B displays a high magnification STEM-HAADF cross-section of the BaTiO₃ layer. Different zones can be observed: while the upper-left squared zone evidences the presence of a high quality, defect free, perovskite structure, the central zone of the image (with darker contrast) shows the presence of a dislocation that transforms a Ba column into a Ti column. Figure 3C–E display GPA analysis performed on CeO₂, LaNiO₃ and BaTiO₃ layers. Colour maps in panels d) and e) show the strain distributions for both in-plane (E_{xx}) and out-of-plane (E_{yy}) directions, calculated from the STEM-HAADF image of panel c). The GPA analysis was performed taken the BaTiO₃ structure as reference. The maps show that the BaTiO₃ layer is not fully strained by the LaNiO₃ layer, as the latter displays an in-plane compressed lattice ($\approx -10\%$) with respect to the former. The presence of defects in the BaTiO₃ layer can be

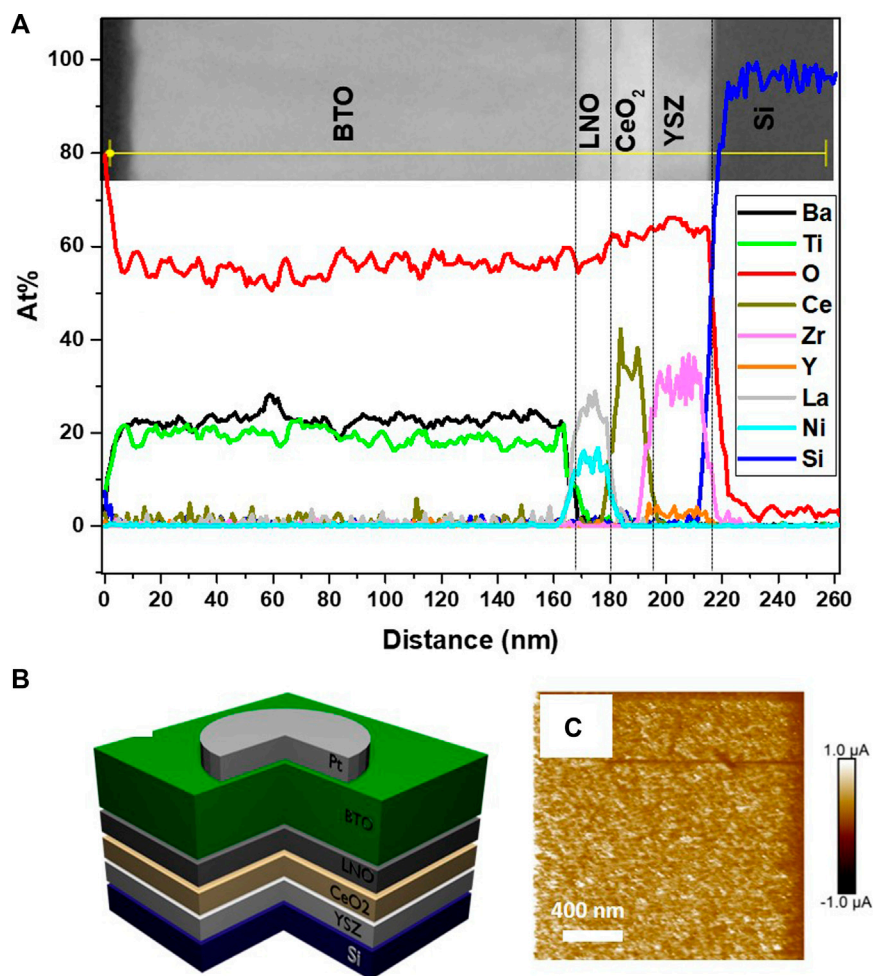


FIGURE 4

(A) Chemical quantification performed on a Si(001)/YSZ/CeO₂/LaNiO₃/BaTiO₃ heterostructure from a STEM-EDS line scan. LaNiO₃ and BaTiO₃ are labelled as LNO and BTO, respectively; (B) Sketch displaying the final device, used for the electrical characterization. LNO and Pt are the bottom and top electrodes, respectively; (C) Conducting atomic force microscopy map recorded on a Si(001)/YSZ/CeO₂/LaNiO₃ structure.

observed in the E_{yy} map, which displays blue-coloured zones where BaTiO₃ is locally strained. Figure 4A shows EDS line scans performed on the Si(001)/YSZ/CeO₂/LaNiO₃/BaTiO₃ heterostructure, together with the corresponding chemical quantifications. YSZ, CeO₂ and BaTiO₃ layers displayed a stoichiometry consistent with the nominal one, while some Ni-deficiency was found for the LaNiO₃ layer.

3.2 Electrical characterization

A sketch of the device used for the electrical characterization is displayed in Figure 4B. The bottom LaNiO₃ electrode was grounded and the electrical stimuli was applied to the top Pt electrode. CAFM experiments were performed on a Si(001)/YSZ/

CeO₂/LaNiO₃ heterostructure (Figure 4C), by applying a 0.25 V DC bias. The measured current values -up to $\approx 1 \mu\text{A}$ -reflect a high conductivity for a perovskite oxide (Sirena et al. (2010)); in addition, the current distribution displays high spatial uniformity. This confirms that our epitaxial LaNiO₃ layer-grown on buffered Si- is an appropriate bottom electrode for our final device, in contrast with the more insulating transport properties observed in polycrystalline LaNiO₃ thin films grown directly on Si (Qiao and Bi (2008)). We also notice that the Ni-deficiency we observed in our LaNiO₃ layer is not detrimental to its high conductivity, in agreement with previous reports (Wakiya et al. (2002)).

The ferroelectric character of the BaTiO₃ layer was tested with different experiments. Figure 5A displays a capacitance-electric field (C-E) curve. The capacitance was acquired with the LCR-

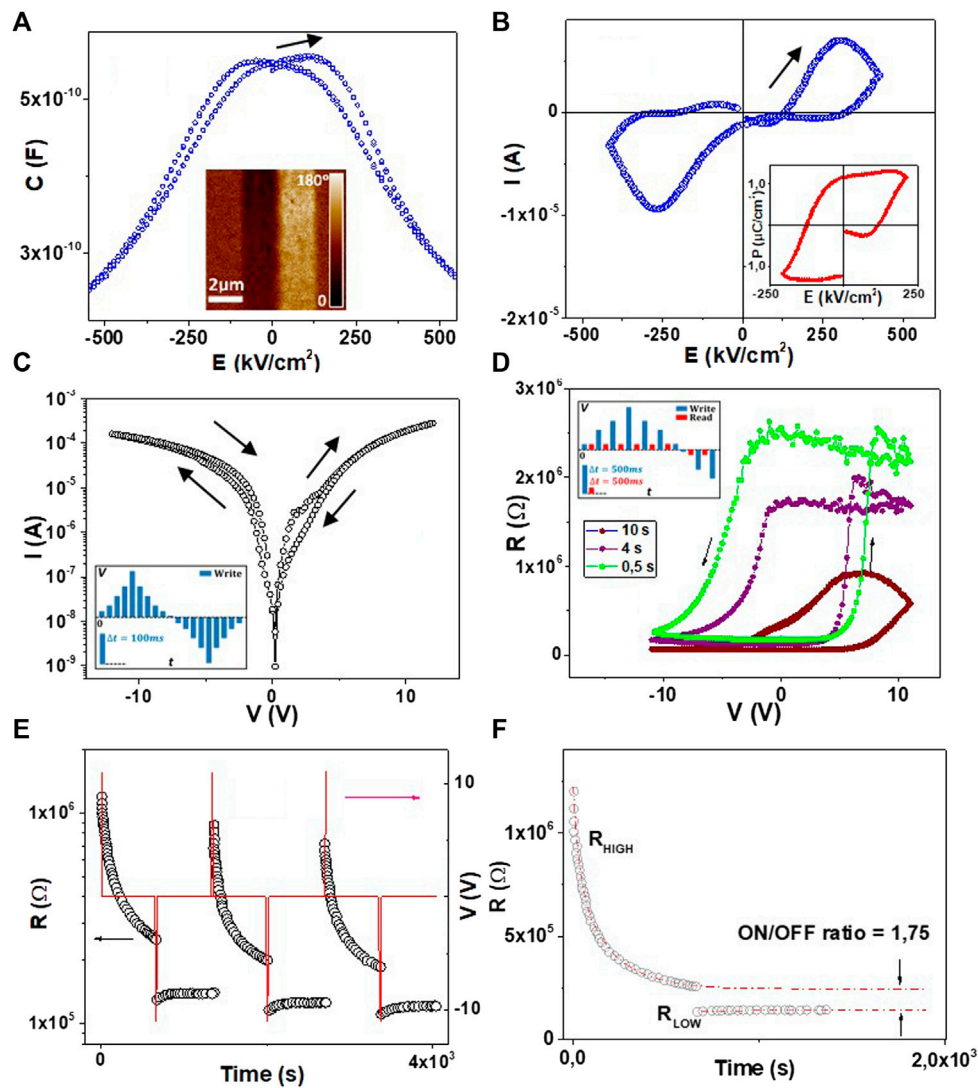


FIGURE 5

(A) Capacitance–electric field (C–E) curve recorded on a Si(001)/YSZ/CeO₂/LaNiO₃/BaTiO₃/Pt device. The inset displays a PFM microscopy phase image, recorded after writing two rectangles with up and down polarization; (B) Current–electric field (obtained by using the PUND protocol, main panel) and polarization–electric field (P–E, inset) curves measured on the same device; (C) Dynamic current–voltage curve recorded on the same device. The presence of hysteresis reflects the existence of memristive behavior. The inset shows the stimulation protocol; (D) Remanent vs. writing voltage loops for the same device, measured for different time-separation between consecutive write pulses. The inset shows the stimulation protocol. See main text for further details; (E) Resistance relaxations measured after the application of single (positive and negative) voltage pulses. We recall the semi-log scale of the plot; (F) Resistance relaxations and exponential fittings for R_{HIGH} and R_{LOW} states, displayed in linear scale. The existence of a mixture of volatile and non-volatile memristive effects is seen.

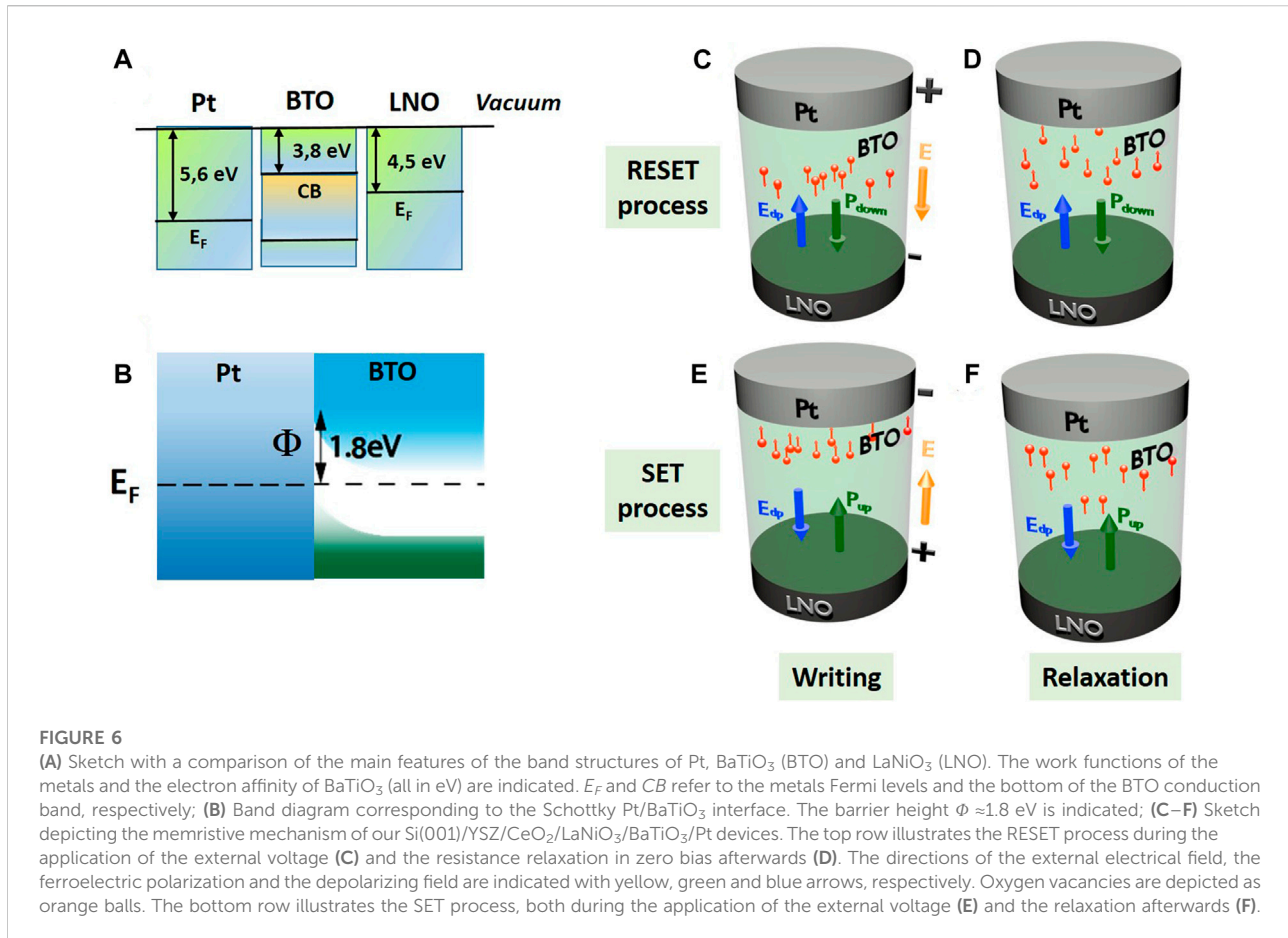
meter by assuming a parallel RC circuit, as it is the standard for low-leakage capacitors. An AC excitation voltage with amplitude 0.5 V and a frequency of 10 kHz was used. The C–E curves displays an hysteretic, butterfly-like shaped evolution, typical of ferroelectric devices. From capacitance measurements, we have extracted the BaTiO₃ dielectric permittivity, obtaining values ranging between ≈ 400 at low frequencies (100 Hz) to ≈ 170 at higher frequencies (10 kHz), in good agreement with previous reports (Thomas et al. (1999)). Figure 5B displays the current–

electric field curve obtained with the Positive-Up Negative-Down (PUND) protocol (a 1 kHz frequency was used), where the presence of ferroelectric displacement peaks are clearly seen. The same figure displays the polarization–electrical field (P–E) loop obtained after the time integration of the current. The P–E loop resembles the one of a standard ferroelectric, despite presenting some asymmetry. This might indicate the existence of an unstable upward polarization (obtained by negatively poling the top electrode), originated by the presence of a

downward internal field due to the asymmetry between both electrodes (Lee et al. (1998); Zhou et al. (2019)). However, this should be accompanied by strong (negative) imprints of both C-V and P-E loops [Lee et al. (1998); Zhou et al. (2019)], which do not seem to be present in Figures 5A,B. Therefore, the asymmetry in the P-E loop should be attributed to other effect, such as the presence of asymmetrical leakage currents Noguchi et al. (2019) which were not fully eliminated during the PUND procedure. Values for the remanent polarization $P_R \approx 1.3 \mu\text{C}/\text{cm}^2$ and coercive field $E_C \approx 120 \text{ kV}/\text{cm}$ are extracted. Finally, the ferroelectric character of the BaTiO₃ layer was confirmed by PFM microscopy, as displayed in the inset of Figure 5A. For this experiment, the polarization of two rectangular zones were written with up and down directions ($\pm 8 \text{ V}$), and the PFM image was recorded afterwards. A clear phase contrast is observed, indicating the anti-parallel polarization directions between both zones. The contrast between both zones was found to decrease in a time scale of $\approx 1 \text{ h}$, indicating the presence of depolarization effects.

We turn now to the memristive properties. Figure 5C shows a dynamic current-voltage (I-V) curve recorded on a LaNiO₃/BaTiO₃/Pt device. The stimulation protocol is displayed in the inset, and consisted on a pulsed ramp of DC voltage pulses, in the range $+12 \text{ V}/-12 \text{ V}$ with a step of 0.2 V and a time-width for each pulse of 100 m . The delay time between consecutive pulses was 0.5 s . The current is measured during the application of each pulse. The I-V curve displays a hysteretic behavior, which is the signature of memristive effects. With positive voltage, the system goes from a low resistance state (LR, higher current) to a high resistance state (HR, lower current), in what is usually called the RESET process. The inverse resistance transition is found for negative voltage (SET process). An ON-OFF ratio of ≈ 10.4 was extracted at 1 V . In order to track the evolution of the remanent resistance as a function of the writing voltage (usually known as Hysteresis Switching Loop, HSL [Rozenberg et al. (2010); Rubi et al. (2013)]), small reading voltages (with amplitude of few hundreds of mV) are usually applied in between writing pulses and the current is recorded in order to extract the remanent resistance of the device without changing it. Given the high remanent resistance values of the device ($\approx 0.5 \text{ G}\Omega$), which turned the low voltage reading of these states unsuitable in DC mode due the low signal-to-noise ratio of the measured currents, we made that measurements in AC mode. For that, we applied DC small reading pulses with a superimposed AC signal (amplitude of $100\text{--}500 \text{ mV}$, frequency of 10 kHz), and the remanent resistance was measured with a LCR-meter assuming a parallel RC circuit. In this case, both write and read pulses were 500 m wide, as depicted in the sketch shown in the inset of Figure 5D). We notice that the assumed circuit is the equivalent representation of a usually more complex primary circuit linked to the different device zones (i.e. each metal/insulator interface is normally assumed as—at least—a capacitor in parallel with a resistor). In this way, the extracted resistance is a function of the AC frequency f), as it includes

capacitive reactances which are f -dependant. We stress that this AC procedure was already shown to be effective to track memristive effects in systems with high DC resistances [Ferreyra et al. (2020a)]. Figure 5D shows HSLs recorded for different time separations between consecutive witting pulses. Each write pulse was followed by a read pulse after a 0.5 s interval, and the next write pulse was applied after an interval Δt_W with respect to the read pulse. We varied Δt_W from 0.5 s to 10 s . Several features are observed: i) as expected from the dynamic I-V curve, the RESET (SET) process is found for positive (negative) voltage; ii) the loops show a squared shape, in consistency with our assumption of only one active memristive interface (BaTiO₃/Pt) [Rozenberg et al. (2010); Ferreyra et al. (2020b)] iii) the ON-OFF ratio—defined as HR/LR—is found to decrease as Δt_W increases, from ≈ 14.7 for $\Delta t_W = 0.5 \text{ s}$ to ≈ 11.2 for $\Delta t_W = 4 \text{ s}$. We notice that for $\Delta t_W = 10 \text{ s}$ the HR state displays a cusp, indicating that it is a non-stable state; iv) both the SET and RESET voltages (V_{SET} and V_{RESET} , respectively) display also a strong dependence with Δt_W . For $\Delta t_W = 0.5 \text{ s}$ we have $V_{SET} \approx 7 \text{ V}$ and $V_{RESET} \approx -5 \text{ V}$ while for $\Delta t_W = 4 \text{ s}$ we have $V_{SET} \approx 5.6 \text{ V}$ and $V_{RESET} \approx -2.3 \text{ V}$. For $\Delta t_W = 10 \text{ s}$ both SET and RESET transition are more gradual and it is therefore difficult to determine a precise value for V_{SET} and V_{RESET} . The features iii) and iv) are a strong indication of the presence of resistance relaxations in absence of external stimuli. To confirm this, we performed the experiments shown in Figure 5E, which consisted on the application of single positive and negative voltage pulses ($+11 \text{ V}$ and -11 V , respectively), followed by the measurement of the time evolution of the remanent resistance (again in AC mode, as in the case of the HSLs). It is found that after the application of a positive voltage pulse the resistance increases, followed by a strong relaxation to lower values. When a negative pulse is applied, the resistance drops and there is a slight resistance recovery afterwards. Figure 5F shows in linear scale both R_{HIGH} and R_{LOW} relaxations corresponding to the first full cycle displayed in semi-log scale in Figure 5E. We fitted the time evolution of both resistance states with a linear combination of exponential functions (red dotted lines). The time-constants related to the HR relaxation are in the range $\approx 0.5\text{--}3 \text{ min}$. It is seen that the R_{HIGH} state is almost fully relaxed at the moment of the application of the next pulse that switches the system to the R_{LOW} state. From the extrapolation of the fittings to higher times we confirm the presence of a non-volatile memristive effect with an ON-OFF ratio of ≈ 1.75 . The described experiments confirm the coexistence of non-volatile and volatile resistive changes with the presence of highly asymmetric relaxations. We notice that resistance relaxations were reported for different ferroelectric memristive devices [Yin et al. (2010); Rubi et al. (2012); Tian et al. (2019); Ferreyra et al. (2020a)] and a phenomenological model to account for this behavior was developed by some of the authors of this paper for symmetric devices Ferreyra et al. (2020a). In the next section, we propose a working model that explains the electrical behavior seen for the asymmetric devices reported here.



3.3 Working model and discussion

In order to explain the evolution of the remanent resistance with the writing voltage and time, several ingredients should be taken into account. We notice that BaTiO₃ is a n-type semiconductor, with electron affinity $E_{ea} \approx 3.8$ eV, which is prone to form Schottky interfaces when placed in contact with high work function (W) metals. In our case, the work functions of Pt and LaNiO₃ are $W \approx 5.6$ and $W \approx 4.5$ eV, respectively (see Figure 6A for a sketch of the corresponding energy band diagrams). For metal-semiconductor contacts, we recall that the height of the interface Schottky barrier Φ_0 is usually estimated as $\Phi_0 = W - E_{ea}$. In our case, it is therefore expected that a significantly higher Schottky barrier will be formed at the BaTiO₃/Pt interface with respect to the BaTiO₃/LaNiO₃ interface ($\Phi_0 \approx 1.8$ eV and 0.7 eV, respectively, see the sketch of Figure 6B). As it is the case of many asymmetric memristive devices driven by interface mechanisms (Rozenberg et al. (2010)), the BaTiO₃/Pt barrier, displaying the highest height, will dominate the electrical transport and the memristive effect.

Upon electrical cycling, the memristive behavior is related to the modulation of the BaTiO₃/Pt interface resistance by different effects. In the first place, we have the influence of the direction of

the electrical polarization on the barrier height (Rault et al. (2013); Hubmann et al. (2016); Pintilie et al. (2007); Farokhipoor and Noheda (2014); Liu et al. (2013). A polarization pointing to the barrier decreases its height according to $\Phi \approx \Phi_0 - \gamma|P|$, where $|P|$ is the polarization absolute value and γ is a constant [see Ferreyra et al. (2020a) and references therein]. This lowers the interface resistance. The inverse effect is found for the opposite polarization direction ($\Phi \approx \Phi_0 + \gamma|P|$). In the second place, we should consider the effect of OV dynamics on the interface resistance. We recall that OV dynamics drives the memristive effect occurring at the interface of several oxide/metal systems Rozenberg et al. (2010); Ferreyra et al. (2019; 2020b). OV are known to locally decrease the resistivity of BaTiO₃ Yang et al. (2004). These vacancies are charged and they can migrate due to the action of electrical fields. This field might come either from the application of external voltage or from the ferroelectric depolarizing field E_{DP} , arising from an incomplete screening by the metallic electrodes of the ferroelectric bound charges. The latter introduces a coupling between the ferroelectric polarization and OV dynamics, as we have previously discussed and modelled for symmetric Pt/PZT/Pt and SrRuO₃/BaTiO₃/SrRuO₃ devices Ferreyra et al. (2020a),

that accounts for resistance relaxations under zero external bias. We recall that the strongest electric field exists close to the BaTiO₃/Pt interface, which is a consequence of its highly resistive nature due to the presence of the highest energy barrier among the two interfaces [Ghenzi et al. \(2010\)](#).

Bearing in mind the previous considerations, the observed phenomenology found in our asymmetric LaNiO₃/BaTiO₃/Pt can be explained as follows (see the sketch displayed in [Figures 6C–E](#)). As we have mentioned, the memristive effect is localized at the BaTiO₃/Pt interface, displaying a high Schottky barrier. When a positive voltage is applied ([Figure 6C](#)), the resistance increases because of the synergistic contribution of the Schottky barrier increase due to the downward switching of the polarization and the removal -by the external electrical field-of OV from the interface to deeper zones of the BaTiO₃ layer. When the external voltage is removed ([Figure 6D](#)), some of these OV are re-injected at the BaTiO₃/Pt interface by the action of E_{DP} -pointing upwards, opposite to the polarization direction-which progressively relaxes the resistance to lower values. As with this polarization direction the Schottky barrier is in its highest value, so is the local electrical field acting on the BaTiO₃/Pt interface and the relaxations are therefore significant. When a negative voltage is applied to the device ([Figure 6E](#)), the resistance decreases as the barrier height decreases with the upward switching of the polarization direction and the injection of OV into the interface, under the action of the external field. After the electrical stimulation is removed ([Figure 6F](#)), some OV will migrate-driven by a downward E_{DP} - from the interface to the deeper zone of the BaTiO₃ layer, producing an increase of the resistance with time. However, as in this situation the polarization points to the interface and this lowers the height of the Schottky barrier, the local electrical field acting at the interface will be milder than in the case with inverse polarization and this explains the more subtle resistance relaxations and the asymmetry found in the resistance relaxations after RESET and SET events.

We recall that [Qian et al. \(2019\)](#) found that two different mechanisms contribute to the electroresistance of BaTiO₃-based ferroelectric memristors. The presence of one or the other mechanism was the time length of the writing pulses. For short pulses (20 μ s) the memristive behavior was dominated by the modulation of the Schottky barrier by the direction of the ferroelectric polarization. For longer pulses (20 s) oxygen vacancy electromigration dominated the change of the Schottky barrier resistance. Our writing pulses present a time-width of 100 ms and are therefore in between the time-widths explored by Qian et al. It is therefore natural to propose, in our case, a coexistence (and competition) between both mechanisms, as was already discussed.

We also notice that our working model assumed that no polarization decay occurs in the time-scale involved in the electrical measurements. This might be concluded from the fact that the observed resistance relaxations present characteristic times of a few minutes, which are significantly faster than the depolarization effects inferred from PFM measurements (typical

times \approx 1 h). However, we notice that the BaTiO₃ boundary conditions (given by the presence or not of Pt top electrode) are different in both experiments, so different depolarizing times might be involved. This suggests that a depolarization effect could be also present in the observed resistance relaxations, an issue that needs to be addressed in the future.

Another possible mechanism that might account for the existence of resistance relaxations in zero external bias is OV back-diffusion [Baeumer et al. \(2015\)](#). This requires the existence of strong OV gradients as those found in systems with memristive mechanisms based on the completion/disruption of OV nanofilaments; for instance Zhang et al. reported OV densities going from $1 \times 10^{19} m^{-3}$ for pristine hafnia to $1 \times 10^{26} m^{-3}$ at the center of an OV filament ([Zhang et al. \(2022\)](#)). This scenario can be disregarded in our case as the I-V curve of [Figure 5C](#) and the remanent resistance loop of [Figure 5D](#) display opposite chiralities to those expected for a filamentary memristive mechanism. Our system displays, instead, an interface-type memristive effect, where OV density profiles present significantly milder gradients [Román Acevedo et al. \(2018\)](#); [Ferreyra et al. \(2020a\)](#). Based on these arguments, we consider that resistance relaxations due to OV back-diffusion are unlikely in our case.

We finally mention that volatile memristive effects driven by the depolarizing field-driven oxygen vacancy dynamics might be mastered by proper interface engineering. We recall that the depolarizing field comes from the incomplete screening of ferroelectric bound charges by the metallic electrodes. The screening capability of the electrode can be controlled by changing the fabrication conditions (for example, its conductivity can be fine-tuned by the deposition and annealing temperature) or by the quality of the interface (i.e. the presence of epitaxy, roughness, interdiffusion). Also, E_{DP} might be tuned by placing ultra-thin insulating barriers in between the ferroelectric and the metal ([Lichtensteiger et al. \(2014\)](#)). By using these knobs the characteristics of the resistance relaxations (for example, their time-constant) might be adapted to the final application needs.

4 Conclusion

In this work we have developed epitaxial BaTiO₃ ferroelectric memristors integrated with silicon. It was found the presence of coexisting volatile and non-volatile memristive effects, with the presence of strongly asymmetric relaxations after SET and RESET events. This phenomenology arises from the combined effect of the interface barrier modulation of the BaTiO₃/Pt interface by the ferroelectric polarization entangled with OV dynamics, the latter driven by the depolarizing field. The results reported here might be relevant for the development of neuromorphic hardware as our devices can electrically replicate, in the same

unit, the behavior of neurons and synapses. Their volatile memristive properties can be useful for the development of applications such as true random generators, selectors in cross-bar arrays, physical unclonable functions and also in reservoir computing (Wang et al. (2020)). Finally, we notice that the integrability of our devices with silicon is of paramount importance to take advantage of existing micro and nanoelectronics technology.

Data availability statement

The raw data supporting the conclusion of this article will be made available by the authors, without undue reservation.

Author contributions

MR fabricated the samples and performed the structural and electrical characterization. MA performed the STEM experiments and GPA analysis. MS conducted the CAFM tests. UL provided the PLD targets. DR conceived the experiments, did the general coordination and supervision of the work and wrote the manuscript.

References

- Baeumer, C., Schmitz, C., Ramadan, A. H. H., Du, H., Skaja, K., Feyer, V., et al. (2015). Spectromicroscopic insights for rational design of redox-based memristive devices. *Nat. Commun.* 6, 8610. doi:10.1038/ncomms9610
- Blom, P. W. M., Wolf, R. M., Cillessen, J. F. M., and Krijn, M. P. C. M. (1994). Ferroelectric Schottky diode. *Phys. Rev. Lett.* 73, 2107–2110. doi:10.1103/physrevlett.73.2107
- Carrero, A., Roman, A., Aguirre, M., and Steren, L. B. (2020). Nanoscale structural characterization of manganite thin films integrated to silicon correlated with their magnetic and electric properties. *Thin Solid Films* 709, 138189. doi:10.1016/j.tsf.2020.138189
- Chanthbouala, A., Garcia, V., Cherifi, R. O., Bouzheouane, K., Fusil, S., Moya, X., et al. (2012). A ferroelectric memristor. *Nat. Mat.* 11, 860–864. doi:10.1038/nmat3415
- Farokhipoor, S., and Noheda, B. (2014). Screening effects in ferroelectric resistive switching of BiFeO₃ thin films. *Appl. Mat.* 2, 056102. doi:10.1063/1.4875355
- Ferreira, C., Acevedo, W. R., Gay, R., Rubi, D., and Sánchez, M. J. (2019). Oxygen vacancy dynamics in redox-based interfaces: Tailoring the memristive response. *J. Phys. D: Appl. Phys.* 53, 015302. doi:10.1088/1361-6463/ab46d3
- Ferreira, C., Rengifo, M., Sánchez, M., Everhardt, A., Noheda, B., and Rubi, D. (2020a). Key role of oxygen-vacancy electromigration in the memristive response of ferroelectric devices. *Phys. Rev. Appl.* 14, 044045. doi:10.1103/physrevapplied.14.044045
- Ferreira, C., Sánchez, M., Aguirre, M., Acha, C., Bengió, S., Lecourt, J., et al. (2020b). Selective activation of memristive interfaces in TaO_x-based devices by controlling oxygen vacancies dynamics at the nanoscale. *Nanotechnology* 31, 155204. doi:10.1088/1361-6528/ab6476
- Garcia, V., Fusil, S., Bouzheouane, K., Enouz-Vedrenne, S., Mathur, N. D., Barthelemy, A., et al. (2009). Giant tunnel electroresistance for non-destructive readout of ferroelectric states. *Nature* 460, 81–84. doi:10.1038/nature08128
- Ghenzi, N., Sánchez, M. J., Gomez-Marlasca, F., Levy, P., and Rozenberg, M. J. (2010). Hysteresis switching loops in ag-manganite memristive interfaces. *J. Appl. Phys.* 107, 093719. doi:10.1063/1.3372617
- Hubmann, A. H., Li, S., Zhukov, S., von Seggern, H., and Klein, A. (2016). Polarisation dependence of Schottky barrier heights at ferroelectric BaTiO₃/RuO₂

Acknowledgments

We acknowledge Marten Piantek, from LMA-INA-UNIZAR, for the PFM measurements. We acknowledge support from ANPCyT (PICT 2019-02781, PICT2020A-00415) and EU-H2020-RISE project MELON (Grant No. 872631).

Conflict of interest

The authors declare that the research was conducted in the absence of any commercial or financial relationships that could be construed as a potential conflict of interest.

Publisher's note

All claims expressed in this article are solely those of the authors and do not necessarily represent those of their affiliated organizations, or those of the publisher, the editors and the reviewers. Any product that may be evaluated in this article, or claim that may be made by its manufacturer, is not guaranteed or endorsed by the publisher.

interfaces: Influence of substrate orientation and quality. *J. Phys. D: Appl. Phys.* 49, 295304. doi:10.1088/0022-3727/49/29/295304

Ielmini, D., and Waser, R. (2016). *Resistive switching: From fundamentals of nanoionic redox processes to memristive device applications*. Weinheim, Germany: Wiley VCH.

Kumar, S., Wang, X., Strachan, J., Yang, Y., and Lu, W. (2022). Dynamical memristors for higher-complexity neuromorphic computing. *Nat. Rev. Mat.* 7, 575–591. doi:10.1038/s41578-022-00434-z

Lee, J., Choi, C. H., Park, B. H., Noh, T. W., and Lee, J. K. (1998). Built-in voltages and asymmetric polarization switching in Pb(Zr, Ti)O₃ thin film capacitors. *Appl. Phys. Lett.* 72, 3380–3382. doi:10.1063/1.121610

Lichtensteiger, C., Fernandez-Pena, S., Weymann, C., Zubko, P., and Triscone, J.-M. (2014). Tuning of the depolarization field and nanodomain structure in ferroelectric thin films. *Nano Lett.* 14, 4205–4211. doi:10.1021/nl404734z

Liu, X., Wang, Y., Burton, J. D., and Tsybal, E. Y. (2013). Polarization-controlled ohmic to Schottky transition at a metal/ferroelectric interface. *Phys. Rev. B* 88, 165139. doi:10.1103/physrevb.88.165139

Lubig, A., Buchal, C., Guggi, D., Jia, C., and Stritzker, B. (1992). Epitaxial growth of monoclinic and cubic ZrO₂ on Si(100) without prior removal of the native SiO₂. *Thin Solid Films* 217, 125–128. doi:10.1016/0040-6090(92)90617-k

Lyu, J., Fina, I., Solanas, R., Fontcuberta, J., and Sánchez, F. (2018). Tailoring lattice strain and ferroelectric polarization of epitaxial BaTiO₃ thin films on Si(001). *Sci. Rep.* 8, 495. doi:10.1038/s41598-017-18842-5

Mehonic, A., and Kenyon, A. (2022). Brain-inspired computing needs a master plan. *Nature* 604, 255–260. doi:10.1038/s41586-021-04362-w

Meyer, R., and Waser, R. (2006). Hysteretic resistance concepts in ferroelectric thin films. *J. Appl. Phys.* 100, 051611. doi:10.1063/1.2337078

Noguchi, Y., Matsuo, I., H., Kitanaka, Y., and Miyayama, M. (2019). Ferroelectrics with a controlled oxygen-vacancy distribution by design. *Sci. Rep.* 9, 4225. doi:10.1038/s41598-019-40717-0

Pintilie, L., Stancu, V., Trupina, L., and Pintilie, I. (2010). Ferroelectric Schottky diode behavior from a SrRuO₃-Pb(Zr_{0.2}Ti_{0.8})O₃-Ta structure. *Phys. Rev. B* 82, 085319. doi:10.1103/physrevb.82.085319

- Pintilie, L., Vrejoiu, I., Hesse, D., LeRhun, G., and Alexe, M. (2007). Ferroelectric polarization-leakage current relation in high quality epitaxial Pb(Zr, Ti)O₃ films. *Phys. Rev. B* 75, 104103. doi:10.1103/physrevb.75.104103
- Qian, M., Fina, I., Sulzbach, M. C., Sánchez, F., and Fontcuberta, J. (2019). Synergetic electronic and ionic contributions to electroresistance in ferroelectric capacitors. *Adv. Electron. Mat.* 5, 1800646. doi:10.1002/aelm.201800646
- Qiao, L., and Bi, X. F. (2008). Strain state, microstructure and electrical transport properties of LaNiO₃ films grown on Si substrates. *J. Phys. D: Appl. Phys.* 41, 195407. doi:10.1088/0022-3727/41/19/195407
- Rault, J. E., Agnus, G., Maroutian, T., Pillard, V., Lecoœur, P., Niu, G., et al. (2013). Interface electronic structure in a metal/ferroelectric heterostructure under applied bias. *Phys. Rev. B* 87, 155146. doi:10.1103/physrevb.87.155146
- Román Acevedo, W., Ferreyra, C., Sánchez, M. J., Acha, C., Gay, R., and Rubi, D. (2018). Concurrent ionic migration and electronic effects at the memristive TiO_x/La_{1/3}Ca_{2/3}MnO_{3-x} interface. *J. Phys. D: Appl. Phys.* 51, 125304.
- Román, A., Rengifo, M., Saleh Medina, L., Reinoso, M., Negri, R., Steren, L., et al. (2017). BaTiO₃ thin films on platinized silicon: Growth, characterization and resistive memory behavior. *Thin Solid Films* 628, 208–213. doi:10.1016/j.tsf.2017.03.038
- Rozenberg, M. J., Sánchez, M. J., Weht, R., Acha, C., Gomez-Marlasca, F., and Levy, P. (2010). Mechanism for bipolar resistive switching in transition-metal oxides. *Phys. Rev. B* 81, 115101. doi:10.1103/physrevb.81.115101
- Rubi, D., Duhalde, S., Terzoli, M., Leyva, G., Polla, G., Levy, P., et al. (2002). Structural and electrical characterization of La_{0.5}Ca_{0.5}MnO₃ thin films grown by pulsed laser deposition. *Phys. B Condens. Matter* 320, 86–89. doi:10.1016/s0921-4526(02)00649-x
- Rubi, D., Gomez-Marlasca, F., Bonville, P., Colson, D., and Levy, P. (2012). Resistive switching in ceramic multiferroic Bi_{0.9}Ca_{0.1}FeO₃. *Phys. B Condens. Matter* 407, 3144–3146. doi:10.1016/j.physb.2011.12.048
- Rubi, D., Tesler, F., Alposta, I., Kalstein, A., Ghenzi, N., Gomez-Marlasca, F., et al. (2013). Two resistive switching regimes in thin film manganite memory devices on silicon. *Appl. Phys. Lett.* 103, 163506. doi:10.1063/1.4826484
- Sawa, A. (2008). Resistive switching in transition metal oxides. *Mater. Today* 11, 28–36. doi:10.1016/s1369-7021(08)70119-6
- Scigaj, M., Chao, C. H., Gázquez, J., Fina, I., Moalla, R., Saint-Girons, G., et al. (2016). High ferroelectric polarization in c-oriented BaTiO₃ epitaxial thin films on SrTiO₃/Si(001). *Appl. Phys. Lett.* 109, 122903. doi:10.1063/1.4962836
- Scigaj, M., Dix, N., Fina, I., Bachelet, R., Warot-Fonrose, B., Fontcuberta, J., et al. (2013). Ultra-flat BaTiO₃ epitaxial films on Si(001) with large out-of-plane polarization. *Appl. Phys. Lett.* 102, 112905. doi:10.1063/1.4798246
- Sirena, M., Zimmers, A., Haberkorn, N., Kaul, E. E., Steren, L. B., Lesueur, J., et al. (2010). Influence of ion implantation on the magnetic and transport properties of manganite films. *Phys. Rev. B* 81, 134439. doi:10.1103/physrevb.81.134439
- Thomas, R., Dube, D., Kamalasanan, M., and Chandra, S. (1999). Optical and electrical properties of BaTiO₃ thin films prepared by chemical solution deposition. *Thin Solid Films* 346, 212–225. doi:10.1016/s0040-6090(98)01772-6
- Tian, J., Tan, Z., Fan, Z., Zheng, D., Wang, Y., Chen, Z., et al. (2019). Depolarization-field-induced retention loss in ferroelectric diodes. *Phys. Rev. Appl.* 11, 024058. doi:10.1103/physrevapplied.11.024058
- Tsymbal, E. Y., and Kohlstedt, H. (2006). Tunneling across a ferroelectric. *Science* 313, 181–183. doi:10.1126/science.1126230
- Wakiya, N., Azuma, T., Shinozaki, K., and Mizutani, N. (2002). Low-temperature epitaxial growth of conductive LaNiO₃ thin films by rf magnetron sputtering. *Thin Solid Films* 410, 114–120. doi:10.1016/s0040-6090(02)00238-9
- Wang, R., Yang, J.-Q., Mao, J.-Y., Wang, Z.-P., Wu, S., Zhou, M., et al. (2020). Recent advances of volatile memristors: Devices, mechanisms, and applications. *Adv. Intell. Syst.* 2, 2000055. doi:10.1002/aisy.202000055
- Weber, M. C., Guennou, M., Dix, N., Pesquera, D., Sánchez, F., Herranz, G., et al. (2016). Multiple strain-induced phase transitions in LaNiO₃ thin films. *Phys. Rev. B* 94, 014118. doi:10.1103/physrevb.94.014118
- Yang, G. Y., Dickey, E. C., Randall, C. A., Barber, D. E., Pinceloup, P., Henderson, M. A., et al. (2004). Oxygen nonstoichiometry and dielectric evolution of BaTiO₃. Part I—improvement of insulation resistance with reoxidation. *J. Appl. Phys.* 96, 7492–7499. doi:10.1063/1.1809267
- Yin, K., Li, M., Liu, Y., He, C., Zhuge, F., Chen, B., et al. (2010). Resistance switching in polycrystalline BiFeO₃ thin films. *Appl. Phys. Lett.* 97, 042101. doi:10.1063/1.3467838
- Yu, S. (2017). *Neuro-inspired computing using resistive synaptic devices*. New York, United States: Springer International Publishing.
- Zhang, K., Ren, Y., Ganesh, P., and Cao, Y. (2022). Effect of electrode and oxide properties on the filament kinetics during electroforming in metal-oxide-based memories. *npj Comput. Mat.* 8, 76. doi:10.1038/s41524-022-00770-2
- Zhou, Y., Wang, C., Lou, X., Tian, S., Yao, X., Ge, C., et al. (2019). Internal electric field and polarization backswitching induced by Nb doping in BiFeO₃ thin films. *ACS Appl. Electron. Mat.* 1, 2701–2707. doi:10.1021/acsaelm.9b00737
- Zhuravlev, M. Y., Wang, Y., Maekawa, S., and Tsymbal, E. Y. (2009). Tunneling electroresistance in ferroelectric tunnel junctions with a composite barrier. *Appl. Phys. Lett.* 95, 052902. doi:10.1063/1.3195075